

## Numerical analysis of radio-frequency sheath-plasma interactions in the ion cyclotron range of frequencies

H. Kohno, J. R. Myra, and D. A. D'Ippolito

Citation: *Physics of Plasmas* (1994-present) **19**, 012508 (2012); doi: 10.1063/1.3677262

View online: <http://dx.doi.org/10.1063/1.3677262>

View Table of Contents: <http://scitation.aip.org/content/aip/journal/pop/19/1?ver=pdfcov>

Published by the [AIP Publishing](#)

---

### Articles you may be interested in

[Radio-frequency sheath-plasma interactions with magnetic field tangency points along the sheath surface](#)  
*Phys. Plasmas* **20**, 082514 (2013); 10.1063/1.4818991

[Characterization and performance of a field aligned ion cyclotron range of frequency antenna in Alcator C-Moda\)](#)  
*Phys. Plasmas* **20**, 056117 (2013); 10.1063/1.4803882

[Blob birth and transport in the tokamak edge plasma: Analysis of imaging data](#)  
*Phys. Plasmas* **13**, 092509 (2006); 10.1063/1.2355668

[Parametric study of two-dimensional potential structures induced by radio-frequency sheaths coupled with transverse currents in front of the Ion Cyclotron Resonance Heating antenna](#)  
*Phys. Plasmas* **13**, 042512 (2006); 10.1063/1.2186530

[Influence of coupling to spectra of weakly damped eigenmodes in the ion cyclotron range of frequencies on parasitic absorption in rectified radio frequency sheaths](#)  
*Phys. Plasmas* **12**, 032505 (2005); 10.1063/1.1851988

---



**PFEIFFER VACUUM**

## VACUUM SOLUTIONS FROM A SINGLE SOURCE

Pfeiffer Vacuum stands for innovative and custom vacuum solutions worldwide, technological perfection, competent advice and reliable service.



# Numerical analysis of radio-frequency sheath-plasma interactions in the ion cyclotron range of frequencies

H. Kohno<sup>1,a)</sup> J. R. Myra,<sup>2</sup> and D. A. D'Ippolito<sup>2</sup>

<sup>1</sup>*Plasma Science and Fusion Center, Massachusetts Institute of Technology, 77 Massachusetts Avenue, Cambridge, Massachusetts 02139, USA*

<sup>2</sup>*Lodestar Research Corporation, 2400 Central Avenue P-5, Boulder, Colorado 80301, USA*

(Received 30 August 2011; accepted 6 December 2011; published online 26 January 2012)

A new finite element numerical scheme for analyzing self-consistent radio-frequency (RF) sheath-plasma interaction problems in the ion cyclotron range of frequencies is applied to various problems represented by simplified models for the tokamak scrape-off layer. The present code incorporates a modified boundary condition, which is called a sheath boundary condition, that couples the radio-frequency waves and sheaths at the material boundaries by treating the sheath as a thin vacuum layer. A series of numerical analyses in one- and two-dimensional domains show several important physical properties, such as the existence of multiple roots, hysteresis effects, presence and characteristics of the sheath-plasma waves, and the phase shift of a reflected slow wave, some of which are newly identified by introducing a spatially varying plasma density and background magnetic field. © 2012 American Institute of Physics. [doi:10.1063/1.3677262]

## I. INTRODUCTION

Radio-frequency (RF) waves in the ion cyclotron range of frequencies (ICRF) have been successfully applied to various heating experiments in fusion plasmas. However, it has been revealed by experimental and theoretical studies that deleterious edge plasma interactions can occur due to various nonlinear mechanisms (see Ref. 1 and the references therein). One of the most important nonlinear effects is RF sheath formation, in which the sheath potential on the walls and limiters of the tokamak device is enhanced by the ICRF waves. RF sheath formation causes various problems including impurity generation by enhanced sputtering and power dissipation in the scrape-off layer (SOL), leading to local hot spots and reduced power, as reviewed in Refs. 1 and 2. In a tokamak device with ICRF heating, RF sheaths are associated with plasma waves, and they are often classified into the broad categories of near- and far-field sheaths.

ICRF antennas are designed to launch a fast wave (FW) with the aim of full absorption of the FW into the core plasma. In this operation, when the antenna current has a component parallel to the magnetic field line intersecting with the antenna, the corresponding electric field component,  $E_{\parallel}$ , of a slow wave (SW) couples with the parallel antenna current and its amplitude is enhanced as a result. In a low-density plasma, the SW with a large-amplitude  $E_{\parallel}$  field propagates until it reaches a material surface and develops net positive direct-current (DC) voltage namely “rectified” sheath potential on the boundary in order to maintain charge ambipolarity.<sup>3–6</sup> Sheaths generated in such a way are referred to as “near-field” or “antenna” sheaths. When the current source is large, the rectified sheath potential on the antenna surface and nearby material boundaries can reach on the order of a kV.

The significance of near-field sheaths was appreciated in the 1980s; from then on, much experimental and theoretical work was conducted at the end of the past century to investigate the effect of sheaths on nearby antenna structures<sup>3–10</sup> and its various secondary effects, such as sheath currents, power dissipation and hot spot formation, and RF sheath-driven edge plasma convection.<sup>11–17</sup> The idea of using insulating limiters to mitigate the RF sheath problem on ICRF antennas was investigated.<sup>18,19</sup> Recently, important evidence for the effects of RF sheaths was observed in experiments on Alcator C-Mod,<sup>20–22</sup> ASDEX-U,<sup>23–25</sup> Tore Supra,<sup>16,17,25–27</sup> and JET.<sup>25,28</sup>

Second, RF sheaths are also generated on material surfaces when a launched FW encounters a wall due to propagation in the SOL or poor central absorption.<sup>29–32</sup> These kinds of sheaths are referred to as “far-field sheaths.” Efforts to develop efficient analytical models to understand the mechanism of far-field sheath formation have continued.<sup>31,32</sup>

There are other interesting phenomena relating to RF sheath-plasma interactions. Particularly, sheath-plasma waves<sup>33,34</sup> and sheath-plasma resonances<sup>32,35,36</sup> were identified as early as the 1960s, and it is still an open question whether these physical phenomena yield significant effects on tokamak operations.

In order to unravel these complicated issues, numerous analytical approaches have been proposed thus far. If one seeks a truly accurate description of RF-sheath interactions, one needs to consider kinetic effects and detailed sheath structures. However, if the research aim is directed at the evaluation of practically important matters, such as the effect of sheaths on waves in the SOL and sheath potentials, these details may be considered as high-order effects. Based on this idea, the “sheath boundary condition (sheath BC)” was proposed in Refs. 31 and 37 for computing RF sheaths in fusion devices. The sheath BC incorporates the effect of the sheath directly into the solution for the RF fields and yields

<sup>a)</sup>Electronic mail: kohno@alum.mit.edu.

various important results, such as threshold-like turn-on of the sheath potential variation, existence of multiple roots, and sheath-plasma resonances.<sup>32,38–41</sup> A similar approach was pursued for modeling sheath formation in plasma processing.<sup>42,43</sup>

For more detailed understanding and predictive capability useful for quantitative evaluation, numerical simulation of sheath-plasma interactions with realistic geometry and plasma profiles is required. In our previous work, we developed a new numerical code, which is named “rfSOL,” based on a nonlinear finite element method, and its accuracy was verified through test problems in one-dimensional (1D) and two-dimensional (2D) domains.<sup>44,45</sup> The objective of the present paper is to further proceed with the numerical analysis of sheath-plasma interactions and generalize previous analytical work, for example, by treating the plasma density and background magnetic field as functions of space. Although our ultimate goal is to understand the complicated sheath physics in realistic tokamak geometry, as a necessary first step, the present work focuses on more fundamental physics with use of a simplified slab geometry and parameter settings which isolate various physical mechanisms.

In this paper, we first present the basic equations and the expressions constituting the sheath BC and then describe the present numerical procedure. After a brief introduction of the rfSOL code, we solve several problems including RF sheath-plasma interactions. In the first problem in a 1D domain, a particular emphasis is placed on a resonance phenomenon generated by a propagating SW confined between a wall-sheath and a reflection point associated with the gradient of plasma density, and the resultant multiple roots. This is followed by the analyses in a 2D slab domain, in which both the thermal and RF sheaths are considered with high and low plasma density values, respectively. Here, an analytical investigation is also conducted to elucidate the characteristic of the wave mode which appears on the sheath-plasma interface. The present numerical analysis is mainly focused on near-field sheath problems.

## II. MODEL FOR RF SHEATH-PLASMA INTERACTIONS

This section summarizes the equations that govern the behavior of plasma waves in the SOL and the interaction between the waves and the sheaths on metal surfaces. All the analyses in this study will be conducted using a cold plasma model due to low plasma temperatures ( $\sim 10$  eV). Also, we assume that only deuterium is considered as an ion species, so that the ion mass is  $m_i = 3.3436 \times 10^{-27}$  kg.

The governing equation for plasma waves in the SOL is a combined form of Maxwell's equations described as

$$\nabla \times \nabla \times \mathbf{E} - \frac{\omega^2}{c^2} \boldsymbol{\varepsilon} \cdot \mathbf{E} - i\omega\mu_0 \mathbf{J}_{\text{ext}} = \mathbf{0}, \quad (1)$$

where the electric field  $\mathbf{E}$  and the external current  $\mathbf{J}_{\text{ext}}$  vary on the RF time scale. Here,  $\omega$  is the applied angular velocity, and  $c$  is the speed of light, having a relation with the dielectric constant  $\varepsilon_0$  and the permeability  $\mu_0$  in vacuum, which is expressed as  $c^2 = (\varepsilon_0\mu_0)^{-1}$ . The dielectric tensor  $\boldsymbol{\varepsilon}$  is given by

$$\boldsymbol{\varepsilon} = (\mathbf{I} - \mathbf{bb})\varepsilon_{\perp} + \mathbf{bb}\varepsilon_{\parallel} + i\mathbf{b} \times \mathbf{I}\varepsilon_{\times}, \quad (2)$$

where  $\mathbf{I}$  is the unit tensor and  $\mathbf{b}$  is the unit vector along the background magnetic field  $\mathbf{B}_0$  ( $\mathbf{b} = \mathbf{B}_0/|\mathbf{B}_0|$ ); the subscript 0 denotes an equilibrium quantity. Here the coefficients  $\varepsilon_{\perp}$ ,  $\varepsilon_{\parallel}$ , and  $\varepsilon_{\times}$  are expressed as follows:

$$\begin{aligned} \varepsilon_{\perp} &= 1 - \sum_j \frac{\omega_{pj}^2}{\omega^2 - \Omega_j^2}, & \varepsilon_{\parallel} &= 1 - \sum_j \frac{\omega_{pj}^2}{\omega^2}, \\ \varepsilon_{\times} &= \sum_j \frac{\omega_{pj}^2 \Omega_j}{\omega(\omega^2 - \Omega_j^2)}, \end{aligned} \quad (3)$$

where  $\omega_{pj}$  is the plasma frequency defined as  $\omega_{pj} = (n_{j0}e^2/\varepsilon_0 m_j)^{1/2}$  and  $\Omega_j = q_j B_0/m_j$ ;  $q_j$  is the electric charge ( $|q_j| = e$ ), and the subscript  $j$  indicates two-species particles, i.e., an ion (i) or an electron (e). Throughout this study, we assume that quasi-neutrality in the plasma is retained, i.e.,  $n_{e0} = n_{i0} = n_0$ .

In the present numerical analysis, the sheath effect is taken into account by means of the sheath BC, which is written as follows:

$$\mathbf{E}_t = \nabla_t \left( \frac{\Delta_{\text{sh}}}{\varepsilon_{\text{sh}}} D_n \right). \quad (4)$$

Here,  $\Delta_{\text{sh}}$  is the time-averaged sheath width,  $\varepsilon_{\text{sh}}$  is the dielectric constant in the sheath (in this study we assume that  $\varepsilon_{\text{sh}} = \varepsilon_0$ ),  $D_n = \mathbf{s} \cdot (\varepsilon_0 \boldsymbol{\varepsilon} \cdot \mathbf{E})$  is the normal component of the electric displacement,  $\mathbf{s}$  is the unit normal vector pointing to the plasma, and the subscript  $t$  denotes the tangential component to the boundary. The sheath BC in the form of Eq. (4) is derived by (1) treating the electron-poor sheath as a thin, vacuum layer, (2) applying the conditions of continuity of  $\mathbf{E}_t$  and  $D_n$  at the sheath-plasma interface, and (3) invoking the electrostatic approximation in the vacuum layer.<sup>31,37</sup> The above boundary condition is described only with the quantities on the plasma side, which makes it unnecessary to resolve the narrow sheath region in numerical analysis.

Assuming that the sheath width satisfies the Child-Langmuir law,<sup>46,47</sup> a useful approximate expression for the sheath width can be written as follows:

$$\Delta_{\text{sh}} = \left( \frac{e C_{\text{sh}}}{\varepsilon_{\text{sh}} T_e} |D_n| \right)^3 \lambda_{\text{De}}^4 + C_{\text{th}} \lambda_{\text{De}}, \quad (5)$$

where  $C_{\text{sh}}$  is an order-unity constant giving the rectification factor,<sup>3</sup>  $T_e$  is the electron temperature,  $\lambda_{\text{De}}$  is the electron Debye length defined as  $\lambda_{\text{De}} = (\varepsilon_0 T_e / n_{e0} e^2)^{1/2}$ , and  $C_{\text{th}}$  is given by

$$C_{\text{th}} = \begin{cases} 0 & \text{for } \theta \leq (m_e/m_i)^{1/2} \\ \left\{ \ln \left[ \left( \frac{m_i}{m_e} \right)^{1/2} \sin \theta \right] \right\}^{3/4} & \text{for } \theta > (m_e/m_i)^{1/2}, \end{cases} \quad (6)$$

where  $\theta$  is the angle between the magnetic field line and the wall. In Eq. (5), the first term, which is nonlinear in the unknown electric field, is dominant for strong RF sheaths, and the Bohm sheath contribution is introduced in the second term as a correction, giving the low voltage limit. Equation

(5) is strictly valid for  $eV_{\text{sh}}/T_e \gg 1$  and  $eV_{\text{sh}}/T_e \ll 1$ , where  $V_{\text{sh}}$  is the instantaneous RF sheath voltage defined by

$$V_{\text{sh}} = \Delta_{\text{sh}} |E_n^{(\text{sh})}| = \Delta_{\text{sh}} \left| \frac{D_n^{(\text{pl})}}{\varepsilon_{\text{sh}}} \right|, \quad (7)$$

with the superscripts sh and pl denoting the quantities in the sheath and plasma, respectively. In intermediate cases,  $eV_{\text{sh}}/T_e \sim 1$ , Eq. (5) provides a smooth and approximate interpolation. The corresponding rectified sheath potential can be obtained from the Child-Langmuir law as follows:

$$V_0 = \frac{T_e}{e} \left( \frac{\Delta_{\text{sh}}}{\lambda_{\text{De}}} \right)^{4/3}, \quad (8)$$

which approaches  $C_{\text{sh}} V_{\text{sh}}$  for  $eV_{\text{sh}}/T_e \gg 1$  and  $V_B$  for  $eV_{\text{sh}}/T_e \ll 1$ , where  $V_B$  is the Bohm sheath potential. This relation is also used in other work (see Refs. 48 and 49).

The numerical simulations undertaken here analyze open field lines limited by two sheaths that are assumed to be uncorrelated for simplicity. Thus, two different values of  $V_0$  can arise at the two termination points resulting in a DC parallel current. This treatment is consistent with fluid-based (short mean free path) modeling of the electron response. Such DC currents have been observed experimentally.<sup>11</sup>

It is important to note that this sheath model has both linear and nonlinear forms. In its most complete form, Eqs. (4) and (5) combine to give a nonlinear sheath BC with  $E_t \propto |D_n|^4$  in the RF-dominated limit. However, in some applications it may be useful to specify the sheath width as an input parameter (typically,  $\Delta_{\text{sh}}$  is of order one to several  $\lambda_{\text{De}}$ ) to get an approximate solution. In this case the sheath BC in Eq. (4) is linear.

In the present model, we assume that the RF waves that enter the core plasma are absorbed there; here we do not take into account low single pass scenarios. In order to assure this approximation, we introduce a damping layer in the vicinity of the core-edge plasma boundary. This can be achieved by defining the electron mass as  $m_e(1 + i\nu/\omega)$  and choosing the artificial collision frequency  $\nu$  to decrease exponentially from the core-edge plasma boundary. As an example,  $\nu$  is described in the following equation for a slab geometry:

$$\nu = \nu_0 \exp\left(-\frac{x - x_{\text{abs}}}{\lambda_\nu}\right), \quad (9)$$

where the domain is  $x > x_{\text{abs}}$ ,  $\nu_0$  is the maximum artificial frequency,  $x_{\text{abs}}$  is the position of the core-side boundary of the plasma, and  $\lambda_\nu$  represents the length of the damping layer. With this procedure, the actual boundary condition on the core side is not important, so that we can impose the conducting-wall boundary condition (conducting-wall BC),  $E_t = 0$ , in this study. This condition, together with the damping layer, is called the “absorbing boundary condition (absorbing BC)” in later numerical analyses.

### III. FINITE ELEMENT DISCRETIZATIONS

In order to numerically solve self-consistent RF sheath-plasma interactions in 1D and 2D domains for ICRF waves, a combined form of Maxwell’s equations and the sheath BC

are discretized by a conventional finite element technique with piecewise (bi)quadratic interpolation functions.<sup>50</sup> One of the most important advantages of the finite element method is that it can easily deal with problems with complicated boundary shapes; this feature is essential for the present study considering that an ultimate goal is to apply the developed numerical scheme to a realistic tokamak divertor geometry. Due to the nonlinearity in the sheath BC, which is brought from the first term in Eq. (5), the nonlinear system of discretized equations is iteratively solved by means of a Newton-Raphson method. Here, focusing on the sparsity of the global matrix, MUMPS (Multifrontal Massively Parallel Solver), is effectively employed for the large-scale computation. The calculations are performed on the Franklin Cray-XT4 computer system at NERSC (National Energy Research Scientific Computing Center). The detailed procedure of the present numerical scheme is described in Refs. 44 and 45 together with its accuracy verification. The developed finite element code is named “rfSOL (integrated code for RF sheath-plasma interactions with a realistic SOL geometry)” with foresight and will be used in Sec. IV to analyze various sheath-plasma interaction problems. The parameters used in the present numerical simulations come from typical ICRF operating conditions in Alcator C-Mod.

## IV. NUMERICAL SIMULATION OF RF SHEATH-PLASMA INTERACTIONS

### A. Multiple roots

Consider first the sheath-plasma interaction in 1D geometry with a spatially varying plasma density profile. Here it is assumed that the sheath is present only on the right boundary ( $x = x_R$ ), while the plasma wave is evanescent due to the absorbing layer close to the left boundary ( $x = x_L$ ). The profile of the plasma density is given by

$$n_0 = \begin{cases} n_L & \text{for } x \leq x_n \\ (n_L - n_R) \exp\left(-\frac{x - x_n}{\lambda_n}\right) + n_R & \text{for } x > x_n, \end{cases} \quad (10)$$

with  $n_L = 1 \times 10^{19} \text{ m}^{-3}$ ,  $n_R = 1 \times 10^{17} \text{ m}^{-3}$ ,  $x_n = 2.8 \text{ m}$ , and  $\lambda_n = 0.02 \text{ m}$  as schematically shown in Fig. 1(a). The calculation domain is defined such that  $x_L = 0 \text{ m}$ ,  $x_{\text{ant}} = 2.96 \text{ m}$  (where an idealized sheet antenna current is flown along the  $y$  direction with its magnitude at  $K$ ), and  $x_R = 3 \text{ m}$ . Note that a sufficiently long distance is provided between the left boundary and the density varying position ( $x = x_n$ ) to assure that the left-going, combined SW and FW wave is smoothly decayed to zero within the absorbing layer and thereby it is not reflected from the left boundary. The background magnetic field is assumed to be spatially constant and slightly tilted to the  $x$  axis;  $B_{0x} = 1.5 \text{ T}$ ,  $B_{0y} = 0 \text{ T}$ , and  $B_{0z} = 4 \text{ T}$ . The other parameters fixed in this analysis are  $f = 80 \text{ MHz}$ ,  $T_e = 10 \text{ eV}$ ,  $k_y = 0 \text{ m}^{-1}$ ,  $k_z = 10.8 \text{ m}^{-1}$ , and  $C_{\text{sh}} = 0.6$ ; the absorbing layer is formed with  $\nu_0 = 3 \times 10^{11} \text{ s}^{-1}$ ,  $x_{\text{abs}} = 0 \text{ m}$ , and  $\lambda_\nu = 0.4 \text{ m}$  [see Eq. (9)]. In this analysis, a uniform mesh which includes 6001 grid points (3000 three-node elements) is used for the finite element discretization.



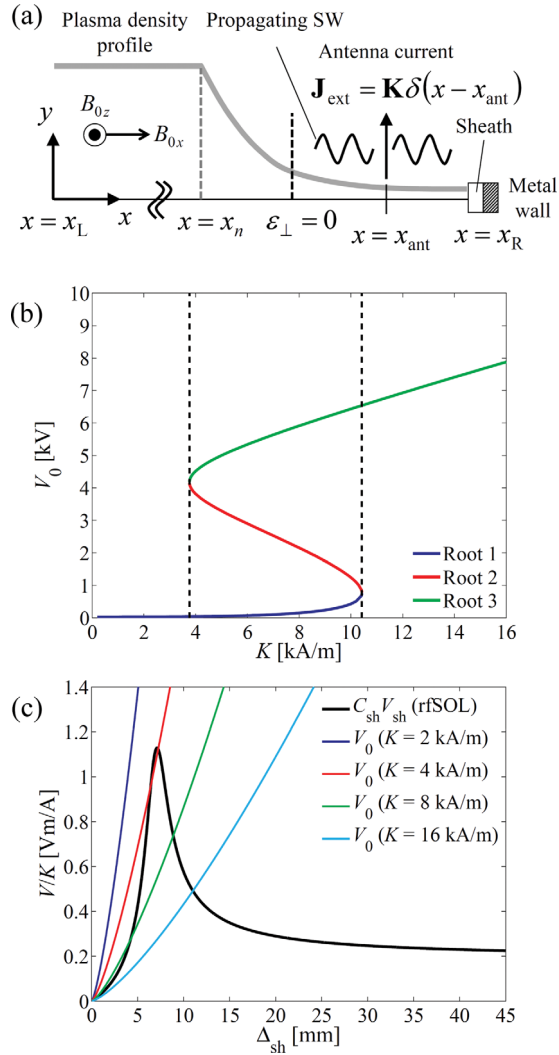


FIG. 1. (Color online) Calculation results of a 1D model problem with a propagating SW confined between a wall-sheath and a reflection point where  $\epsilon_{\perp} = 0$ : (a) schematic of the problem; (b) root structure for the rectified sheath potential as a function of the antenna current, obtained from the nonlinear 1D rfSOL code (root 1 - bottom; root 2 - middle; root 3 - top); and (c) graphical solution for different values of the antenna current; here the thick black curve is obtained by the linear 1D rfSOL, and the curves for  $V_0$  correspond to the cases where (from left to right)  $K = 2, 4, 8$ , and  $16$  kA/m.

While it is not possible to provide a completely satisfactory description of tokamak edge geometry in our 1D and 2D simulations, the following qualitative correspondences can be made. The  $y$  and  $z$  coordinates correspond to the poloidal and toroidal directions, respectively, which are taken to be periodic along the two directions transverse to the density gradients. (In the calculations for the 1D domain, we have set  $k_y = 0$  and  $B_{0y} = 0$  for simplicity.) Interpretation of the  $x$  coordinate is more complicated. It can be thought of as approximately the radial (i.e.,  $R$ ) coordinate in a slab idealization of the toroidal machine and also the direction normal to the conducting outer wall. A small tilt of the background magnetic field in the  $x$  direction allows the field lines to intersect the walls and thus produce RF sheaths at these boundaries. An important fact in this problem is that a SW is confined between a wall-sheath and a reflection point where  $\epsilon_{\perp} = 0$  due to the varying plasma density profile, which can cause a

resonant phenomenon, as will be seen below. It is also a case of some practical importance since this situation can occur in realistic tokamak plasmas. Using the SW dispersion relation,<sup>51</sup> the position where  $\epsilon_{\perp} = 0$  is calculated at  $x_n = 2.88$  m.

Figure 1(b) shows the variation of the rectified sheath potential at the sheath as a function of the antenna current obtained using the fully nonlinear rfSOL code in which the sheath width is obtained as part of the solution. It is interesting to see that there are three different roots for the antenna current in a range between  $K = K_{\text{crit1}} = 3.8$  kA/m (lower critical current) and  $K = K_{\text{crit2}} = 10.4$  kA/m (higher critical current). The mechanism for the root jumping can involve hysteresis. For example, root 1 jumps to root 3 at  $K = K_{\text{crit2}}$  for increasing antenna current, while root 3 jumps to root 1 at  $K = K_{\text{crit1}}$  for decreasing antenna current. The fact that the lower critical current exists is the consequence of having the dissipation in the form of complex electron mass:  $m_e(1 + i\nu/\omega)$ .

The reason that we have multiple solutions in this problem is apparent from the graphical solution<sup>40</sup> in Fig. 1(c). Here the thick black curve corresponds to the RF sheath potential at the sheath ( $V_0 \sim C_{\text{sh}} V_{\text{sh}}$ ), which is obtained by employing the linear 1D rfSOL code with “specified” sheath widths. The colored curves correspond to the sheath potential  $V_0$  computed from the Child-Langmuir law [see Eq. (8)]. Notice that the vertical axis of the plot shows the voltage value normalized by the antenna current; therefore, one can draw an infinite number of Child-Langmuir curves depending on the value of  $K$ . The intersections of the curves correspond to the self-consistent solutions (i.e., self-consistent sheath widths and potential values).

In Fig. 1(c), we see a resonance behavior in the numerical solution when the sheath width approaches 7 mm. This occurs due to the phase matching of the SW confined between a wall-sheath on one side and a reflection point where  $\epsilon_{\perp} = 0$  on the other side. Each of the curves for  $K = 2$  and  $16$  kA/m has one intersection point with the thick black curve, while the other curves shown here have three intersection points. The number of the intersection points is suddenly increased from one to three at the apex of the resonance curve, i.e., when the antenna current is slightly increased from  $3.8$  kA/m. This behavior corresponds to the root jumping at  $K = K_{\text{crit1}}$  observed in Fig. 1(b). It is seen that the graphical solution agrees well with the self-consistent nonlinear numerical result for a large value of  $V_0$ . For example, the thick black curve on the right-hand side intersects with the curve for  $K = 16$  kA/m at  $V/K = 0.49$  Vm/A, which gives  $V = 7.8$  kV and agrees with the numerical result in Fig. 1(b).

## B. Sheath-plasma waves in 2D slab geometry

Next, let us consider analyzing sheath-plasma interaction problems in 2D geometry using the 2D rfSOL code. Figure 2 shows the problem definition which corresponds to a simplified geometry of the edge plasma region including an antenna in the poloidal cross-section of a tokamak. Here, the electric field in the 2D slab geometry is numerically solved subject to the sheath BC on the right-hand side, the

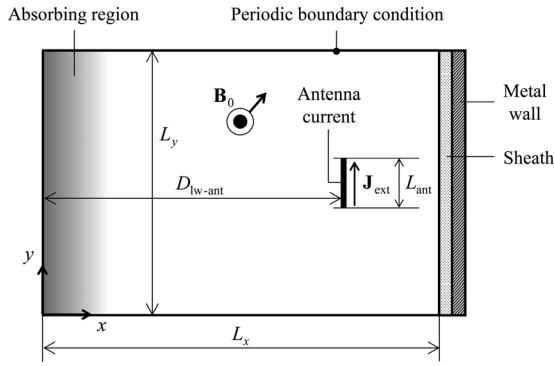


FIG. 2. Infinitely long slab model defined on the 2D space.

absorbing BC on the left-hand side (if necessary, i.e., in the case where waves propagate to the left boundary), and a periodic boundary condition at the top and bottom of the domain. The antenna surface current is given by a sine function in the  $y$  direction in such a way that the value at both ends of the antenna,  $y = L_y/2 \pm L_{\text{ant}}/2$ , is zero, which is achieved using the following expression:

$$\mathbf{J}_{\text{ext}} = K(y)\delta(x - D_{\text{lw-ant}})e^{i(k_z z - \omega t)}\mathbf{e}_y, \quad (11)$$

where  $\mathbf{e}_y$  is the unit vector in the  $y$  direction, and

$$K(y) = \frac{K_{\text{max}}}{2} \left\{ \sin \left[ \pi \left( \frac{2y - L_y + L_{\text{ant}}}{L_{\text{ant}}} - \frac{1}{2} \right) \right] + 1 \right\}. \quad (12)$$

As the first problem in the 2D domain, consider the case where the plasma density and background magnetic field are assumed to be constant over the domain and only the thermal contribution in the sheath BC plays a role in the sheath-plasma interaction (due to a small electric field). The calculation domain and antenna position are determined such that  $L_x = 0.6$  m,  $L_y = 0.4$  m,  $L_{\text{ant}} = 0.05$  m, and  $D_{\text{lw-ant}} = 0.57$  m. The plasma density and background magnetic field are fixed at  $n_0 = 2 \times 10^{18} \text{ m}^{-3}$ ,  $B_{0x} = 1.5$  T,  $B_{0y} = 0.5$  T, and  $B_{0z} = 4$  T. In this analysis, the toroidal wavenumber component is fixed at  $10.8 \text{ m}^{-1}$ , the antenna surface current  $K_{\text{max}}$  is 1 A/m, the electron temperature is 10 eV, and the applied frequency is 80 MHz. For these parameters, both the fast and slow waves do not propagate in the cold plasma according to the local dispersion relation.<sup>51</sup> Thus, it is not necessary to form an absorbing layer on the left-hand side of the domain since the electric field far away from the antenna is sufficiently damped; only the conducting-wall BC,  $\mathbf{E}_t = 0$ , on the left boundary ( $x = 0$ ) suffices. For the finite element discretization, a partly uniform mesh is used, which includes  $901 \times 1281$  grid points, ( $420 \times 640$  nine-node elements in  $0 \leq x \leq D_{\text{lw-ant}}$  and  $30 \times 640$  elements in  $D_{\text{lw-ant}} \leq x \leq L_x$  are used in the  $x$  and  $y$  directions, respectively.)

Figures 3(a) and 3(b) show the filled contour plots of the real part of the parallel electric field component ( $E_{\parallel} = \mathbf{E} \cdot \mathbf{b}$ ), which are obtained by imposing the conducting-wall and thermal sheath BCs on the right boundary, respectively. Here, the antenna and magnetic field lines are also superimposed on the plots with black lines. In Fig. 3(a), the large-amplitude electric field only exists in the vicinity of the current source since the

plasma waves are evanescent. However, the electric field distribution changes significantly when the boundary condition is replaced with the thermal sheath BC as seen in Fig. 3(b). Clearly, a wave mode is observed along the sheath surface. This particular form of wave was confirmed in previous experimental and analytical studies<sup>32–34,40</sup> and is called the “sheath-plasma wave (SPW).” The SPW observed here looks quite regular in distribution, and it is localized in the vicinity of the sheath. The source of the SPW may be attributed to the large-amplitude electric field, which is localized at the intersections between the sheath and the magnetic field lines penetrating through the antenna. The results in Fig. 3 are consistent with the fact that the SPW is a mode of the combined sheath-plasma system; the SPW disappears in the limit  $\Delta_{\text{sh}} \rightarrow 0$ .

In order to understand the relation between the wavenumber of the SPW and the plasma density on the sheath, one can apply the theory of an electrostatic 2D sheath mode. Consider a homogeneous plasma with constant density and a uniform constant magnetic field in the equilibrium state. The presence of wave patterns on the sheath invokes the mode  $\sim \exp(i\mathbf{k} \cdot \mathbf{x})$ . Further, assume that the electrostatic model is valid (i.e.,  $\mathbf{E} = -\nabla\Phi = -i\mathbf{k}\Phi$ ). Then for a constant sheath width, one gets

$$1 = i\Delta_{\text{sh}}\mathbf{s} \cdot (\boldsymbol{\varepsilon} \cdot \mathbf{k}). \quad (13)$$

The wavenumber components must also satisfy the electrostatic dispersion relation in the plasma, which is given by

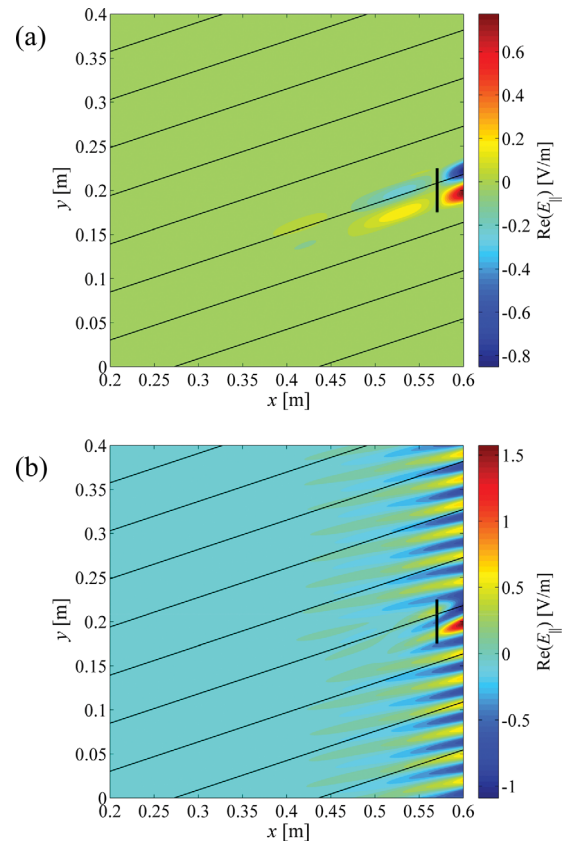


FIG. 3. (Color online) Filled contour plots of the real part of the parallel electric field component for a spatially constant background magnetic field under the conducting-wall BC (a) and the thermal sheath BC (b).

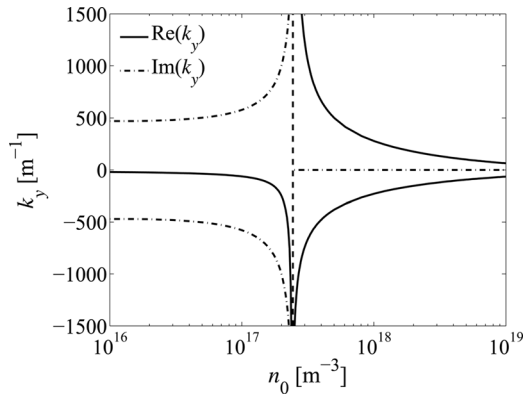


FIG. 4. Plot of the real and imaginary parts of  $k_y$  at the sheath-plasma interface as functions of the plasma density. The vertical dashed line shows the density value of the lower hybrid resonance. Due to field line tilt, positive and negative  $\text{Re}(k_y)$  are not exactly symmetric. In fact, just below the lower hybrid resonance, both (highly evanescent) roots have  $\text{Re}(k_y) < 0$ .

$$k_{\perp}^2 \varepsilon_{\perp} + k_{\parallel}^2 \varepsilon_{\parallel} = 0. \quad (14)$$

Consequently, one can solve Eqs. (13) and (14) to determine  $k_x$  and  $k_y$  for given  $\omega$  and  $k_z$ . The Newton-Raphson method can be applied for this nonlinear calculation, or Eqs. (13) and (14) may be solved for  $k_y$  by eliminating  $k_{\parallel}$  and  $k_x$  analytically. If this is done, a quadratic equation results with two roots for  $k_y$ .

Figure 4 shows the variations of the real and imaginary parts of  $k_y$  at the sheath-plasma interface as functions of the plasma density with semi-logarithmic scale for the horizontal axis. Here it is assumed that the sheath is aligned parallel with the  $y$  axis, and the vertical dashed line indicates the plasma density corresponding to the lower hybrid resonance ( $\varepsilon_{\perp} = 0$ ; this density value is called the lower hybrid density  $n_{\text{LH}}$  hereafter). Notice that the variation pattern becomes completely opposite at the lower hybrid density. According to this result, the SPW only appears for the plasma density greater than the lower hybrid density since for  $n_0 < n_{\text{LH}}$ ,  $\text{Im}(k_y)$  greatly exceeds  $\text{Re}(k_y)$ , so that the SPW is quickly damped before its wave motion can emerge as a propagating wave along the sheath. For the density value considered here, the corresponding wavelength is calculated using one root at  $3.6 \times 10^{-2}$  m, which agrees well with the numerical result shown in Fig. 3(b). Although not shown in this paper, the wavenumber component of the SPW parallel to the sheath surface also depends on several other quantities, such as the angle and magnitude of the poloidal component of the background magnetic field, and the electron temperature.<sup>45</sup> Note that the presence of field line tilt breaks the symmetry of the problem in the  $y$  direction. Consequently, Fig. 4 is not symmetric about  $k_y = 0$ , although it is approximately so when the density value is far away from the lower hybrid resonance.

As a last example of this section, we consider the case where the background magnetic field has a variation along the thermal sheath surface. Here the  $x$  component of the background magnetic field is given by

$$B_{0x} = \frac{2}{3} \tilde{B}_{0x} \left[ 1 - \frac{1}{2} \cos\left(\frac{2y}{L_y} \pi\right) \right], \quad (15)$$

where  $\tilde{B}_{0x} = 1.5$  T, while the other components are fixed at  $B_{0y} = 0.5$  T and  $B_{0z} = 4$  T. All other input parameters are unchanged from the previous example. Figure 5 shows the filled contour plot of the real part of the parallel electric field component. It is observed that the wavelength and spatial decay of the SPW vary along the sheath surface; the wavelength becomes shorter with distance from the antenna, and a corresponding spatial decay in  $y$  occurs as the SPW propagates along the sheath. It is also interesting to see that the decay length in  $x$  (i.e., the penetration into the plasma) of the SPW becomes shorter with a decrease in the SPW wavelength.

### C. Nonlinear sheath-plasma interactions in 2D slab geometry

The discussion for the 2D domain so far focused on the linear sheath-plasma interaction, and the numerical results were given for the plasma density greater than the lower hybrid density where the conventional SW was evanescent and only the SPW propagated. This section aims to solve the case of propagating SWs with nonlinear sheath interactions in 2D slab geometry. Since the SW electric field component parallel to the magnetic field line can be driven by the parallel component of the antenna current, the resulting sheath potential can be quite large ( $\sim$  kV), which enhances the wall sputtering. The calculation model used here is the same as in Sec. IV B except that the thermal sheath is now replaced with an RF sheath which includes the electric field contribution.

The calculation domain and antenna position are determined such that  $L_x = 0.7$  m,  $L_y = 0.3$  m,  $L_{\text{ant}} = 0.05$  m, and  $D_{\text{lw-ant}} = 0.65$  m. The plasma density and background magnetic field are assumed to be constant;  $n_0 = 1 \times 10^{17} \text{ m}^{-3}$ , and  $B_{0x} = 1.5$  T,  $B_{0y} = 0.5$  T, and  $B_{0z} = 4$  T. For this density value, the SW propagates in the cold plasma according to the result of the local dispersion relation.<sup>51</sup> Thus, one is required to form an absorbing layer on the left-hand side of the domain; here it is formed with  $\nu_0 = 3 \times 10^{11} \text{ s}^{-1}$ ,  $x_{\text{abs}} = 0$  m, and  $\lambda_{\nu} = 0.05$  m. The other parameters fixed in this analysis are  $f = 80$  MHz,  $T_e = 10$  eV,  $k_z = 10.8 \text{ m}^{-1}$ , and  $C_{\text{sh}} = 0.6$ . A uniform mesh which includes  $1261 \times 1041$

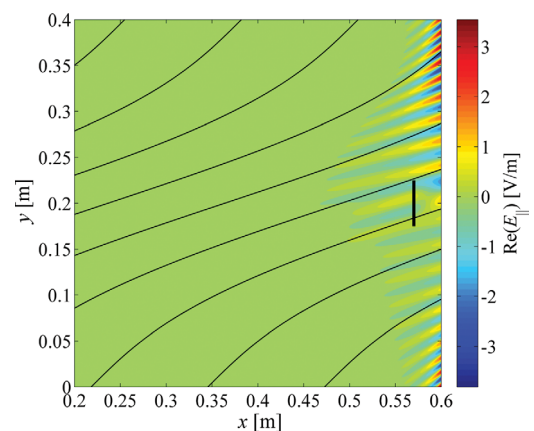


FIG. 5. (Color online) Filled contour plot of the real part of the parallel electric field component for a spatially varying background magnetic field under the thermal sheath BC.



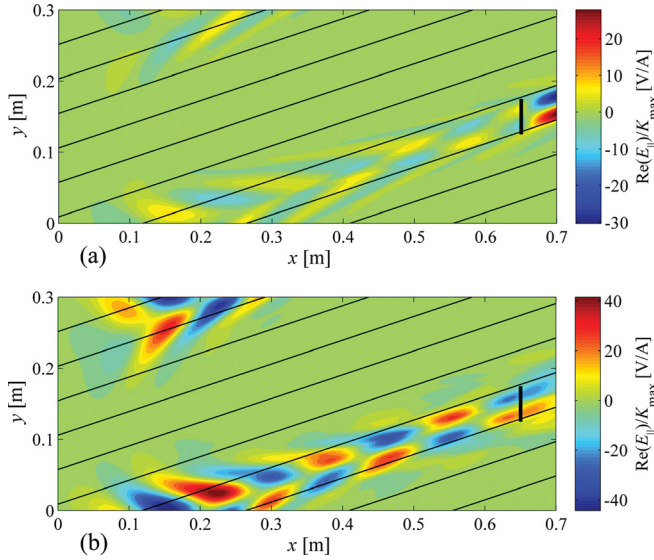


FIG. 6. (Color online) Filled contour plots of the real part of the parallel electric field component for a spatially constant background magnetic field under the nonlinear sheath BC for  $K_{\max} = 1$  A/m (a) and  $K_{\max} = 160$  A/m (b).

grid points ( $630 \times 520$  nine-node elements) is used for the finite element discretization. In this analysis, the strength of the antenna current, specifically the value of  $K_{\max}$  in Eq. (12), is varied in the range 1 – 320 A/m.

Figures 6(a) and 6(b) show the filled contour plots of the real part of the parallel electric field component, which is normalized by dividing it by the maximum surface current value, for  $K_{\max} = 1$  and 160 A/m, respectively. It is observed that the SWs are propagating along the field lines in the form of resonance cones,<sup>38</sup> but the distribution patterns are clearly different between the two cases; the normalized wave amplitude in the edge plasma volume is enhanced for a larger value of  $K_{\max}$ . One of the reasons for this phenomenon may be explained by the phase shift in the reflected wave from the wall behind the antenna. This is demonstrated below using a simplified model.

Suppose that a SW is propagating in a low density plasma with a constant uniform background magnetic field (for simplicity here taken as  $\mathbf{B}_0 = B_{0x}\mathbf{e}_x$ , where  $\mathbf{e}_x$  is the unit vector in the  $x$  direction). Further, assume that the sheath is formed on the right-most boundary ( $x = x_R$ ) of the plasma-filled domain; thus, there are incident (from left to right) and reflected (from right to left) waves in the vicinity of the metal wall. Here the perpendicular wavenumber components are imposed such that  $k_y = 0$  and  $k_z = k_t$ , so that one can write  $k_{\parallel} = k_x$  and  $k_{\perp} = k_t$ . For this simplified condition, the electric field in the plasma is expressed as

$$\mathbf{E} = (C_1 \tilde{\mathbf{E}}_1 e^{ik_t x} + C_2 \tilde{\mathbf{E}}_2 e^{-ik_t x}) e^{i(k_t z - \omega t)}, \quad (16)$$

where  $C_1$  and  $C_2$  are arbitrary constants, and  $\tilde{\mathbf{E}}_1$  and  $\tilde{\mathbf{E}}_2$  are the polarization eigenvectors corresponding to  $k_x = \pm k_t$ , respectively. Now consider the two opposite limits in the sheath BC:  $\Delta_{\text{sh}} \rightarrow 0$  and  $\Delta_{\text{sh}} \rightarrow \infty$ . In the former and latter cases, the sheath BC reduces to the conducting-wall and insulating BCs (i.e.,  $\mathbf{E}_t = \mathbf{0}$  and  $D_n = 0$ ), respectively, for a finite wave source. In the SW limit, the electric fields in the plasma corresponding to the two limits are

$$\mathbf{E} = \begin{cases} C_1 [\tilde{\mathbf{E}}_1 e^{ik_t x} - \tilde{\mathbf{E}}_2 e^{ik_t (2x_R - x)}] e^{i(k_t z - \omega t)} & (\Delta_{\text{sh}} \rightarrow 0) \\ C_1 [\tilde{\mathbf{E}}_1 e^{ik_t x} + \tilde{\mathbf{E}}_2 e^{ik_t (2x_R - x)}] e^{i(k_t z - \omega t)} & (\Delta_{\text{sh}} \rightarrow \infty) \end{cases}. \quad (17)$$

Observe that the signs of the reflected wave are opposite. In other words, a phase shift of  $\pi$  occurs. This is the same result found in the 2D resonance cone analysis.<sup>38</sup> A more detailed derivation is described in the Appendix.

In the simulation, the waves that reflect from the right boundary and return to the plasma interfere with the left-going waves launched directly by the antenna. The interference will be constructive or destructive depending on the parallel wavenumber component, the distance between the antenna and the wall along the field line, and whether there is a phase shift on reflection. For fixed wavenumber and antenna-to-wall distance, the interference behavior is determined by the phase shift caused by the presence of the sheath. The phase shift should occur smoothly between the two opposite limits in the sheath BC.

Figure 7 shows the variations of the normalized normal component of the electric displacement on the sheath surface for five different antenna current values. It is seen that the normalized quantity decreases with an increase in the antenna current, which is a similar behavior to the result shown in Ref. 44 (or Ref. 45) in a 1D domain, indicating that the sheath BC approaches the quasi-insulating limit. Figure 8 shows the variations of the rectified sheath potential corresponding to the five antenna currents. It is seen that the maximum sheath potential value increases with an increase of the antenna current.

For the cases explored in this section (in particular, Fig. 8), the maximum sheath potential depends on the gradient of the antenna current; specifically, the rectified sheath potential decreases with an increase in the antenna length for a given sinusoidal profile. The reason for this is as follows. One can show that when the wavelength of the excited waves and the antenna length  $L_{\text{ant}}$  are both short compared with  $c/\omega$  (as is the case here), the mechanism by which the antenna excites waves is primarily electrostatic. In the

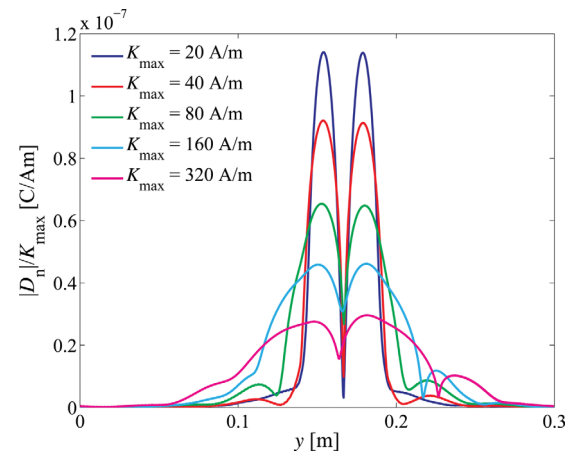


FIG. 7. (Color online) Normalized normal component of the electric displacement vs.  $y$  at the right boundary for five different antenna current values. Note that the largest peak value of  $|D_n|/K_{\max}$  is for the case where  $K_{\max} = 20$  A/m, while the smallest peak value is for  $K_{\max} = 320$  A/m.



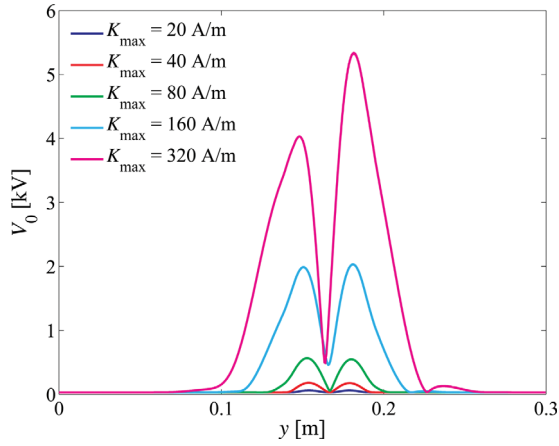


FIG. 8. (Color online) Rectified sheath potential vs.  $y$  at the right boundary for five different antenna current values. The peak potential of about 5 kV occurs for the case where  $K_{\max} = 320$  A/m and decreases monotonically with  $K_{\max}$ .

electrostatic limit, charges build up on the antenna from  $\nabla \cdot \mathbf{J}_{\text{ant}} \sim J_{\text{ant}}/L_{\text{ant}}$  (assuming a half-wave length sinusoidal current profile along the antenna). The electric fields are proportional to the antenna charge, and this results in an inverse scaling of  $E_{\parallel}$  and reduction of the maximum sheath potential with  $L_{\text{ant}}$ . In general, the scaling for the sheath voltage is more complicated because the character of the sheath changes to quasi-insulating as  $V_0$  increases.

Actual ICRF antennas have straps  $\sim 10$  times longer than the simulated current sheet. Thus, the case we studied is not realistic for modeling the electromagnetic coupling on the scale of the whole antenna; it is intended as a demonstration of physical mechanisms (resonance cone propagation, nonlinear sheath formation, and nonlinear phase shifts). However, it is interesting to note that real antennas can have cm-scale sub-structures (e.g., corners and radially protruding elements).<sup>23</sup> Such structures carry RF parallel currents, accumulate RF charge, and excite slow waves on the cm scale. As a matter of speculation, these may not be unlike our simulation in some respects. Quantitative evaluation of the nonlinear threshold for sheath effects in experiments will have to await more realistic simulations.

## V. CONCLUSIONS

In this paper, we presented several new properties caused by self-consistent RF sheath-plasma interactions for ICRF waves using the rfSOL code. The present numerical results that contribute to understanding RF sheath-plasma interaction problems are summarized as follows.

First, in the 1D analysis employing a varying plasma density profile, multiple roots were found in the process of increasing the antenna current. With the help of a graphical solution, it was confirmed that the presence of the multiple roots is attributed to a combination of box-type resonance effects of the confined propagating slow wave together with nonlinearity of the sheath boundary condition. It was also clarified that the root jumping mechanism can involve hysteresis.

In a 2D slab geometry, sheath-plasma waves were identified, and their characteristics were investigated through the electrostatic 2D sheath mode analysis. An important consequence is that a sheath-plasma wave, propagating along the sheath boundary but localized to it, only appears if the plasma density is greater than the lower hybrid density. It was found that the wavelength of the sheath-plasma wave depends on the plasma density. In addition, it was revealed for a varying background magnetic field that its wavelength also depends on the angle (with the wall) and magnitude of the poloidal component of the background magnetic field and its decay length into the plasma becomes shorter with a decrease in its wavelength.

When the plasma density is lower than that at the lower hybrid resonance, it was demonstrated in a 2D slab geometry that the electric field distribution pattern of propagating slow waves varies with an increase in the antenna current. An analytical investigation with a simplified condition showed that the phase shift resulting from the wave interaction with the sheath can be the cause for this variation. Specifically, the sheath boundary condition makes a transition from reflecting (low voltage, small sheath width) to quasi-insulating (high voltage, large sheath width) limits as the sheath width, and hence sheath voltage, increases. Further, it was observed that the normal electric displacement normalized by the maximum antenna current decreases with the antenna current, which demonstrates the validity of the quasi-insulating limit.

## ACKNOWLEDGMENTS

We would like to thank P. T. Bonoli and the RF SciDAC project for supporting this work. This work was supported by the U.S. DOE Contracts DE-FG02-91ER54109, DE-FC02-01ER54648, DE-FG02-97ER54392, and DE-FC02-05ER54823.

## APPENDIX: PHASE SHIFT OF THE REFLECTED WAVE

In this appendix, we derive Eq. (17) from Eq. (16) together with the simplified assumptions in detail. In the SW limit the electric field is governed by the following equation:

$$\begin{pmatrix} \varepsilon_{\perp} - n_{\parallel}^2 & n_{\perp} n_{\parallel} \\ n_{\perp} n_{\parallel} & \varepsilon_{\parallel} - n_{\perp}^2 \end{pmatrix} \begin{pmatrix} E_z \\ E_x \end{pmatrix} = \begin{pmatrix} 0 \\ 0 \end{pmatrix}. \quad (\text{A1})$$

Here, let us specify that  $\tilde{E}_{z1} = \tilde{E}_{z2} = 1$ . Then the expressions of  $\tilde{E}_{x1}$  and  $\tilde{E}_{x2}$  are given by

$$\tilde{E}_{x1} = -\tilde{E}_{x2} = -\frac{\varepsilon_{\perp} - n_{\parallel}^2}{n_{\perp} n_r}, \quad (\text{A2})$$

where  $n_r = ck_r/\omega$  and  $n_{\perp} = ck_t/\omega$ .

Now consider the two opposite limits in the sheath BC;  $\Delta_{\text{sh}} \rightarrow 0$  and  $\Delta_{\text{sh}} \rightarrow \infty$ . In the former and latter cases, the sheath BC reduces to the conducting-wall and insulating BCs, respectively, for a finite wave source. In this analysis they are simplified to  $E_z = 0$  and  $E_x = 0$ , so that one gets

$$\begin{aligned}
C_1 \tilde{E}_{z1} e^{ik_r x_R} + C_2 \tilde{E}_{z2} e^{-ik_r x_R} &= 0 \quad (\text{for conducting BC}) \\
C_1 \tilde{E}_{x1} e^{ik_r x_R} + C_2 \tilde{E}_{x2} e^{-ik_r x_R} &= 0 \quad (\text{for insulating BC})
\end{aligned}
\tag{A3}$$

Substituting the expressions for the polarization eigenvector components into the above equations, we obtain the expressions of  $C_2$  with respect to  $C_1$  in both limits. Consequently, the electric fields are written as shown in Eq. (17).

- <sup>1</sup>J. R. Myra, D. A. D'Ippolito, D. A. Russell, L. A. Berry, E. F. Jaeger, and M. D. Carter, *Nucl. Fusion* **46**, S455 (2006).
- <sup>2</sup>J.-M. Noterdaeme and G. Van Oost, *Plasma Phys. Controlled Fusion* **35**, 1481 (1993).
- <sup>3</sup>J. R. Myra, D. A. D'Ippolito, and M. J. Gerver, *Nucl. Fusion* **30**, 845 (1990).
- <sup>4</sup>F. W. Perkins, *Nucl. Fusion* **29**, 583 (1989).
- <sup>5</sup>R. Van Nieuwenhove and G. Van Oost, *J. Nucl. Mater.* **162–164**, 288 (1989).
- <sup>6</sup>R. Chodura and J. Neuhauser, in *Proceedings of the 16th European Conference on Controlled Fusion and Plasma Heating, Venice* (European Physical Society, Petit-Lancy, Switzerland, 1989), Vol. 13B, Part III, p. 1089; R. Chodura, *Fusion Eng. Des.* **12**, 111 (1990).
- <sup>7</sup>M. Bureš, J. Jacquinet, K. Lawson, M. Stamp, H. P. Summers, D. A. D'Ippolito, and J. R. Myra, *Plasma Phys. Controlled Fusion* **33**, 937 (1991).
- <sup>8</sup>D. A. D'Ippolito, J. R. Myra, M. Bureš, and J. Jacquinet, *Plasma Phys. Controlled Fusion* **33**, 607 (1991).
- <sup>9</sup>M. Bureš, J. J. Jacquinet, M. F. Stamp, D. D. R. Summers, D. F. H. Start, T. Wade, D. A. D'Ippolito, and J. R. Myra, *Nucl. Fusion* **32**, 1139 (1992).
- <sup>10</sup>D. A. D'Ippolito and J. R. Myra, *Phys. Plasmas* **3**, 420 (1996).
- <sup>11</sup>R. Van Nieuwenhove and G. Van Oost, *Plasma Phys. Controlled Fusion* **34**, 525 (1992).
- <sup>12</sup>D. A. D'Ippolito, J. R. Myra, J. Jacquinet, and M. Bures, *Phys. Fluids* **B5**, 3603 (1993).
- <sup>13</sup>J. R. Myra, D. A. D'Ippolito, and Y. L. Ho, *Fusion Eng. Des.* **31**, 291 (1996).
- <sup>14</sup>J. R. Myra and D. A. D'Ippolito, *Phys. Plasmas* **3**, 699 (1996).
- <sup>15</sup>D. A. D'Ippolito, J. R. Myra, J. H. Rogers, K. W. Hill, J. C. Hosea, R. Majeski, G. Schilling, J. R. Wilson, G. R. Hanson, A. C. England, and J. B. Wilgen, *Nucl. Fusion* **38**, 1543 (1998).
- <sup>16</sup>M. Bécoulet, L. Colas, S. Pécou, J. Gunn, Ph. Ghendrih, A. Bécoulet, and S. Heuraux, *Phys. Plasmas* **9**, 2619 (2002).
- <sup>17</sup>L. Colas, L. Costanzo, C. Desgranges, S. Brémond, J. Bucalossi, G. Agarici, V. Basiuk, B. Beaumont, A. Bécoulet, and F. Nguyen, *Nucl. Fusion* **43**, 1 (2003).
- <sup>18</sup>R. Majeski, P. H. Probert, T. Tanaka, D. Diebold, R. Breun, M. Doczy, R. Fonck, N. Hershkowitz, T. Intrator, G. McKee, P. Nonn, J. Pew, and J. Sorensen, *Fusion Eng. Des.* **24**, 159 (1994).
- <sup>19</sup>J. R. Myra, D. A. D'Ippolito, J. A. Rice, and C. S. Hazelton, *J. Nucl. Mater.* **249**, 190 (1997).
- <sup>20</sup>B. Lipschultz, D. A. Pappas, B. LaBombard, J. E. Rice, D. Smith, and S. J. Wukitch, *Nucl. Fusion* **41**, 585 (2001).
- <sup>21</sup>S. J. Wukitch, T. Graves, Y. Lin, B. Lipschultz, A. Parisot, M. Reinke, P. T. Bonoli, M. Porkolab, I. H. Hutchinson, E. Marmor, and the Alcator C-Mod Team, in *Proceedings of the 21st IAEA Fusion Energy Conference*, Chengdu, China (IAEA, Vienna, 2006), paper IAEA-CN-149-F7/1-6.
- <sup>22</sup>S. J. Wukitch, Y. Lin, B. LaBombard, B. Lipschultz, D. Whyte, and the Alcator C-Mod Team, in *Proceedings of the 22nd IAEA Fusion Energy Conference*, Geneva, Switzerland (IAEA, Vienna, 2008), paper IAEA-CN-165-EX/P6-23.
- <sup>23</sup>V. V. Bobkov, F. Braun, R. Dux, A. Herrmann, L. Giannone, A. Kallenbach, A. Krivska, H. W. Müller, R. Neu, J.-M. Noterdaeme, T. Pütterich, V. Rohde, J. Schweinzer, A. Sips, I. Zammuto, and ASDEX Upgrade Team, *Nucl. Fusion* **50**, 035004 (2010).
- <sup>24</sup>V. V. Bobkov, F. Braun, L. Colas, R. Dux, H. Faugel, L. Giannone, A. Herrmann, A. Kallenbach, H. W. Müller, R. Neu, J.-M. Noterdaeme, Th. Pütterich, G. Siegl, E. Wolfrum, and ASDEX Upgrade Team, *J. Nucl. Mater.* **415**, S1005 (2011).
- <sup>25</sup>L. Colas, A. Ekedahl, M. Goniche, J. P. Gunn, B. Nold, Y. Corre, V. Bobkov, R. Dux, F. Braun, J.-M. Noterdaeme, M.-L. Mayoral, K. Kirov, J. Mailloux, S. Heuraux, E. Faudot, J. Ongena, *ASDEX Upgrade Team, and JET-EFDA contributors, Plasma Phys. Controlled Fusion* **49**, B35 (2007).
- <sup>26</sup>L. Colas, V. Basiuk, B. Beaumont, A. Bécoulet, G. Bosia, S. Brémond, M. Chantant, F. Clairet, A. Ekedahl, E. Faudot, A. Géraud, M. Goniche, S. Heuraux, G. T. Hoang, G. Lombard, L. Millon, R. Mitteau, P. Mollard, K. Vulliez, and the Tore Supra team, *Nucl. Fusion* **46**, S500 (2006).
- <sup>27</sup>L. Colas, J. P. Gunn, I. Nanobashvili, V. Petržílka, M. Goniche, A. Ekedahl, S. Heuraux, E. Joffrin, F. Saint-Laurent, C. Balorin, C. Lowry, and V. Basiuk, *J. Nucl. Mater.* **363–365**, 555 (2007).
- <sup>28</sup>P. Jacquet, L. Colas, M.-L. Mayoral, G. Arnoux, V. Bobkov, M. Brix, P. Coad, A. Czarnicka, D. Dodt, F. Durodie, A. Ekedahl, D. Frigione, M. Fursdon, E. Gauthier, M. Goniche, M. Graham, E. Joffrin, A. Korotkov, E. Lerche, J. Mailloux, I. Monakhov, C. Noble, J. Ongena, V. Petržílka, C. Portafaix, F. Rimini, A. Sirinelli, V. Riccardo, Z. Vizvary, A. Widdowson, K.-D. Zastrow, and *JET EFDA Contributors, Nucl. Fusion* **51**, 103018 (2011).
- <sup>29</sup>T. Hellsten and M. Laxåback, *Phys. Plasmas* **12**, 032505 (2005).
- <sup>30</sup>J. Hosea, R. E. Bell, B. P. LeBlanc, C. K. Phillips, G. Taylor, E. Valeo, J. R. Wilson, E. F. Jaeger, P. M. Ryan, J. Wilgen, H. Yuh, F. Levinton, S. Sabbagh, K. Tritz, J. Parker, P. T. Bonoli, R. Harvey, and *NSTX Team, Phys. Plasmas* **15**, 056104 (2008).
- <sup>31</sup>J. R. Myra, D. A. D'Ippolito, and M. Bures, *Phys. Plasmas* **1**, 2890 (1994).
- <sup>32</sup>D. A. D'Ippolito, J. R. Myra, E. F. Jaeger, and L. A. Berry, *Phys. Plasmas* **15**, 102501 (2008).
- <sup>33</sup>G. Bekefi, *Radiation Processes in Plasmas* (Wiley, New York, 1966).
- <sup>34</sup>J. R. Myra, D. A. D'Ippolito, D. W. Forslund, and J. U. Brackbill, *Phys. Rev. Lett.* **66**, 1173 (1991).
- <sup>35</sup>K. Takayama, H. Ikegami, and S. Miyazaki, *Phys. Rev. Lett.* **5**, 238 (1960).
- <sup>36</sup>R. L. Stenzel, *Phys. Rev. Lett.* **60**, 704 (1988).
- <sup>37</sup>D. A. D'Ippolito and J. R. Myra, *Phys. Plasmas* **13**, 102508 (2006).
- <sup>38</sup>J. R. Myra and D. A. D'Ippolito, *Phys. Rev. Lett.* **101**, 195004 (2008).
- <sup>39</sup>D. A. D'Ippolito and J. R. Myra, *Phys. Plasmas* **16**, 022506 (2009).
- <sup>40</sup>J. R. Myra and D. A. D'Ippolito, *Plasma Phys. Controlled Fusion* **52**, 015003 (2010).
- <sup>41</sup>D. A. D'Ippolito and J. R. Myra, *Phys. Plasmas* **17**, 072508 (2010).
- <sup>42</sup>E. F. Jaeger, L. A. Berry, J. S. Tolliver, and D. B. Batchelor, *Phys. Plasmas* **2**, 2597 (1995).
- <sup>43</sup>M. D. Carter, P. M. Ryan, D. Hoffman, W. S. Lee, D. Buchberger, and V. Godyak, *J. Appl. Phys.* **100**, 073305 (2006).
- <sup>44</sup>H. Kohno, J. R. Myra, and D. A. D'Ippolito, *Comput. Phys. Commun.* (submitted).
- <sup>45</sup>H. Kohno, "Numerical analysis of radio-frequency sheath-plasma interactions in the ion cyclotron range of frequencies," Sc.D. thesis, MIT, 2011.
- <sup>46</sup>C. D. Child, *Phys. Rev. (Ser. I)* **32**, 492 (1911).
- <sup>47</sup>I. Langmuir, *Phys. Rev.* **21**, 419 (1923).
- <sup>48</sup>M. A. Lieberman, *IEEE Trans. Plasma Sci.* **16**, 638 (1988).
- <sup>49</sup>V. A. Godyak and N. Sternberg, *Phys. Rev. A* **42**, 2299 (1990).
- <sup>50</sup>K. J. Bathe, *Finite Element Procedures* (Prentice-Hall, Englewood Cliffs, NJ, 1996).
- <sup>51</sup>T. H. Stix, *Waves in Plasmas* (Springer-Verlag, New York, 1992).